Mechanics Research Communications 124 (2022) 103914

Contents lists available at ScienceDirect

Mechanics Research Communications

journal homepage: www.elsevier.com/locate/mechrescom

Different erosion and entrainment mechanisms in snow avalanches

Xingyue Li [a], Betty Sovilla [b], Camille Ligneau [b], Chenfanfu Jiang [c], Johan Gaume [b,d,*]

[a] Department of Geotechnical Engineering, College of Civil Engineering, Tongji University, Shanghai, 200092, China
[b] WSL Institute for Snow and Avalanche Research, SLF, Flüelastrasse 11, Davos, 7260, Switzerland
[c] Department of Mathematics, University of California, Los Angeles, MS 7619E, Los Angeles, 90095, CA, USA
[d] School of Architecture, Civil and Environmental Engineering, Swiss Federal Institute of Technology, Lausanne, Rte Cantonale, Lausanne, 1015, Switzerland

ARTICLE INFO

Keywords:
Erosion
Entrainment
Snow avalanche
MPM

ABSTRACT

Erosion significantly affects the dynamics of gravity-driven mass flows. In snow avalanches, the snow cover can be substantially eroded but only partially entrained, however, there are very limited investigations to substantiate this difference. Here, we study various erosion and entrainment behaviors in snow avalanches using the material point method (MPM), finite strain elastoplasticity and critical state soil mechanics. With varied snow properties, distinct erosion patterns are obtained and analyzed with the mass change rate. When there is significant eroded and entrained mass, properties of released snow and erodible bed snow have clear correlations with the eroded mass, but not with the entrained mass, disclosing the difference in erosion and entrainment. Both enhanced and inhibited avalanche mobilities due to erosion and entrainment are captured under different conditions of snow properties and lengths of release and erodible zones. These new insights may stimulate the development of advanced erosion and entrainment models for large-scale avalanches.

1. Introduction

Entrainment is a common and crucial process observed from a wide spectrum of geophysical flows including rock avalanches, debris flows, and landslides. Snow avalanches, as one of the most frequent and dangerous natural hazards in cold mountainous regions, are also affected by entrainment. According to field observations, the mass of a single avalanche can grow by a factor of 12 due to entrainment [1]. The mass change influences the dynamics of snow avalanches by changing their flow velocity, flow height and runout distance [1]. It has been recognized that entrainment and erosion may either restrict or enhance the avalanche motion [2], while only positive correlation between entrained mass and runout distance has been reported for snow avalanches [3,4]. For a dry cohesionless granular avalanche, it was found that the avalanche mobility can vary significantly depending on the erodible layer thickness and the slope angle [5,6].

According to Gauer and Issler [7], the breaking up of the snow cover into smaller pieces (ranging from snow grains to blocks) is termed *erosion*, and the process whereby the eroded snow becomes part of the flowing avalanche is called *entrainment*. In line with this definition, the mass of entrained snow is less than or at most equal to the mass of eroded snow. In existing studies on mass change of snow avalanches, entrainment and erosion are often used interchangeably [2,8], which might be under the assumption that all the eroded snow is entrained. However, recent analysis on an approximate momentum balance of field avalanches by Issler et al. [9] indicates that the snow cover can be considerably eroded but only partially entrained into the flow. Distinguishing entrainment from erosion not only leads to more accurate prediction of the mass increase of the flow, but also gives information on snow cover fragments remaining on the slope, which can potentially be entrained by a subsequent avalanche. Nonetheless, no quantitative difference between entrainment and erosion has been reported for snow avalanches, as the differentiation is challenging in both real measurements and laboratory experiments. As direct measurement of entrainment in nature and of its effect on flow dynamics is very difficult [10], numerical approaches serve as an alternative tool in assessing entrainment quantitatively.

The mass growth of an avalanche is generally ascribed to frontal entrainment and basal erosion [7,11,12], while the mass reduction is normally attributed to tail deposition [9,13]. However, the temporal evolution of entrainment, erosion and deposition rate has been rarely discussed, limiting the evaluation of mass change throughout the entire flowing process. In addition, snow properties (e.g. temperature) at release and along the track do greatly affect entrainment [14]. Nevertheless, to the best knowledge of the authors, quantitative assessment of mass change (i.e. erosion, entrainment, deposition) with various release properties and flow types has never been explored under well-controlled conditions.

* Corresponding author.
E-mail address: johan.gaume@epfl.ch (J. Gaume).

https://doi.org/10.1016/j.mechrescom.2022.103914
Received 18 August 2021; Received in revised form 5 February 2022; Accepted 1 June 2022
Available online 9 June 2022
0093-6413/© 2022 The Authors. Published by Elsevier Ltd. This is an open access article under the CC BY-NC-ND license (http://creativecommons.org/licenses/by-nc-nd/4.0/).

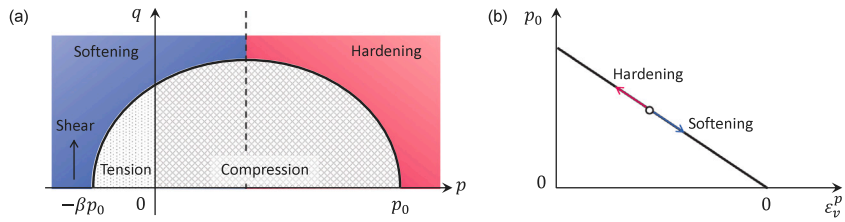

Fig. 1. Illustration of (a) the adopted yield surface in Eq. (2) and (b) the hardening law in Eq. (3).

This study aims at offering new insights into the mechanisms and effects of erosion and entrainment processes in snow avalanches with the help of advanced numerical simulations. Based on the material point method (MPM) and an elastoplastic constitutive law developed for snow [15,16], snow avalanches in different flow regimes have been captured with various release properties [17,18]. With further consideration of an erodible bed in this study, the effect of released snow type on entrainment and erosion can be conveniently explored, and the temporal variation of mass change in the erodible zone can be quantitatively analyzed, as detailed in Section 3.1. In addition, the difference of entrainment and erosion will be visualized and related to the snow properties at the release and at the erodible bed in Section 3.2. Furthermore, opposite effects of erosion on the avalanche mobility will be discussed in Section 3.3, from the perspectives of momentum change and runout distance.

2. Methodology and model setup

To investigate erosion and entrainment by snow avalanches, the material point method [19] and a finite-strain elastoplastic model [15] are adopted in this study. The hybrid Eulerian/Lagrangian MPM does not need to trace neighboring particles compared with pure Lagrangian methods like the discrete element method (DEM), and avoids the mesh distortion issue in comparison with continuum approaches such as the finite element method (FEM). Meanwhile, the elastoplastic model encompasses the mixed-mode failure of snow, strain softening, plastic compaction and various flow regimes of snow avalanches.

MPM uses particles (or material points) to trace mass, momentum, and deformation gradient, and adopts background grids and interpolation functions to solve the motion of the particles and update their states. Given a continuous material, MPM firstly discretizes the material to particles. The mass and velocities of the particles are then transferred to the grid nodes. The grid forces coming from elastic stresses of the particles can then be calculated, and the grid velocities can be updated considering the new grid forces. Given the updated grid velocities, the deformation gradients of the particles can be updated. Finally, the grid velocities are transferred back to the particles to get the new particle velocities, according to which the particle positions are updated. With the Lagrangian particles and the Eulerian grids, MPM does not need Lagrangian mesh connectivity and implicitly handles discontinuous processes such as fractures and breakage. This provides great flexibility in modeling large deformation problems such as those found in snow avalanches.

The large-strain elastoplastic constitutive model adopted in this study is developed for snow [15], with the stress–strain relation expressed as:

$$\boldsymbol{\sigma} = \frac{1}{J}\frac{\partial \Psi}{\partial \boldsymbol{F}_E}\boldsymbol{F}_E^T \tag{1}$$

where $\boldsymbol{\sigma}$ is the Cauchy stress, Ψ is the elastoplastic potential energy density, $\boldsymbol{F}_E$ denotes the elastic part of the deformation gradient $\boldsymbol{F}$, and $J = \det(\boldsymbol{F})$. The elastoplastic constitutive model consists of a yield surface, a hardening law, and an associative flow rule.

The adopted yield surface is a cohesive Cam-clay yield criterion, illustrated in Fig. 1a and defined in the $p-q$ space as:

$$y(p,q) = (1+2\beta)q^2 + M^2(p+\beta p_0)(p-p_0) \tag{2}$$

where p is the pressure and q is the von Mises stress. $p > 0$ and $p < 0$ denote compression and tension, respectively, while $q > 0$ indicates shear. The consolidation pressure is denoted as p_0, and the tensile strength is βp_0, where β reflects the internal cohesion of the material. Given a constant consolidation pressure p_0, the larger the cohesion β, the higher the tensile strength βp_0. The friction is controlled by M, which could be related to the internal friction angle of a material according to well-designed experiments [20,21]. When the $p-q$ state is inside or on the yield surface (i.e. $y(p,q) \le 0$), the material has purely elastic deformation. Otherwise, plasticity occurs, and a hardening law and a flow rule need to be defined.

The following hardening law (illustrated in Fig. 1b) is adopted to expand or shrink the yield surface in order to account for the hardening or softening of the material:

$$p_0 = K\sinh(\xi \max(-\epsilon_v^p, 0)) \tag{3}$$

where K denotes the bulk modulus, ξ is the hardening factor, and ϵ_v^p is the volumetric plastic strain. During the simulation, K and ξ are constant, while ϵ_v^p changes according to the plastic volume. When the plastic volume increases ($\dot{\epsilon}_v^p > 0$), p_0 decreases, giving softening of the material and allowing fracture to occur. Otherwise ($\dot{\epsilon}_v^p < 0$), p_0 increases and the material is hardened. The hardening factor ξ controls the speed of the hardening during the plastic stage. A larger ξ leads to faster growth of stress, reflecting a more brittle material.

Following Gaume et al. [15], an associative plastic flow rule [22,23] is used in this study. The adopted flow rule follows the principle of maximum plastic dissipation and gives a plastic flow that maximizes the plastic dissipation rate. The cohesive Cam-clay yield surface and the associative flow rule in this study have been recently proven to be satisfactory for simulation of porous brittle solids such as snow [24]. More details of the MPM and the constitutive model can be found in [15,25,26].

The model setup in our MPM simulations consists of an ideal concave slope, a release zone and an erodible bed, as illustrated in Fig. 2. Similar setups were used in both numerical investigations [27] and experimental studies [28,29] of erosion and scour behavior of granular materials, where a slope with constant inclination was normally used. As second-order polynomial curves can represent complex and irregular tracks while offering ideal and well-controlled conditions, they have been widely used in investigations of snow avalanches [30–32]. The slope in Fig. 2 is a second-order polynomial fitting of the 2D projected avalanche path at Weissfluh-Northridge, Davos, Switzerland [33]. The friction coefficient of the slope is fixed to 0.5, around which the behavior of real avalanches can be reasonably captured [17]. To save computational cost, the majority of the simulations in this study were conducted in 2D, while four simulations were performed in 3D to be compared with the 2D simulations for confirmation of consistency. The grid size of the simulations is 0.1 m, resulting in simulations with good accuracy and at a reasonable computational cost. The time step is set to 4.6 $\times 10^{-4}$ s, constrained by the Courant–Friedrichs–Lewy (CFL) condition and the elastic wave speed for simulation stability. In 2D simulations, each grid cell is filled with 4 material points (or particles), while a grid cell in 3D simulations contains 6 particles.

In this study, four sets of released snow properties (i.e. friction M, cohesion β, hardening factor ξ, and initial consolidation pressure

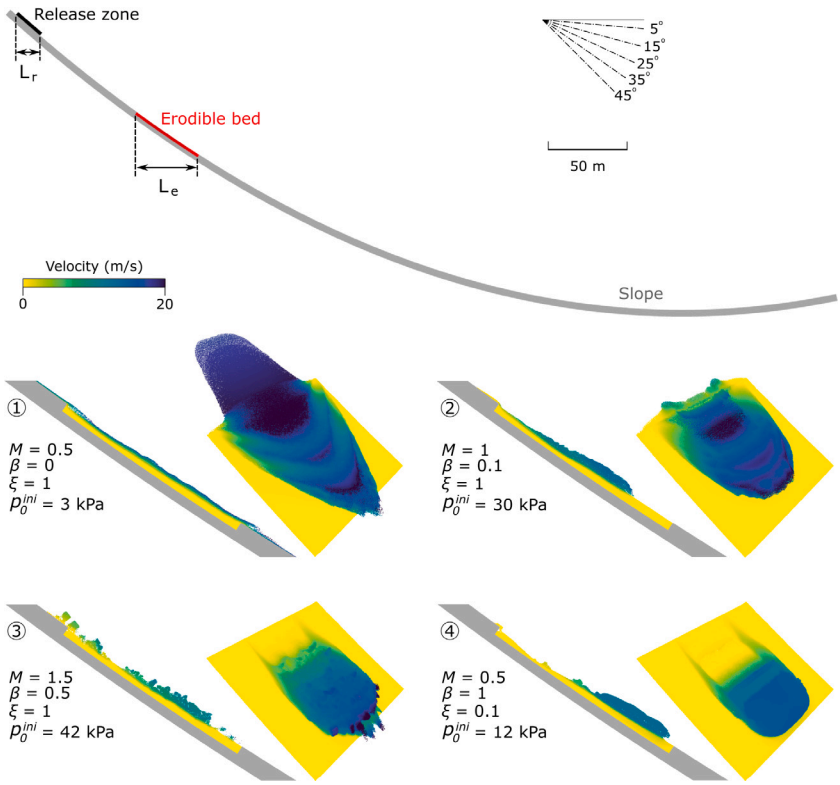

Fig. 2. MPM modeling of snow avalanche erosion and entrainment in 4 scenarios with different properties of the released snow. M is the friction coefficient, β is the cohesion coefficient, ξ is the hardening factor, p_0^{ini} is the initial consolidation pressure. The bed snow properties (M = 0.7, β = 0.4, ξ = 0.1, p_0^{ini} = 12 kPa) in the four cases are identical. Videos of the simulated 4 scenarios in 2D and 3D can be found in the supplementary material.

p_0^{ini}) listed in Fig. 2 are applied to obtain avalanches with distinct features and investigate their effect on entrainment and erosion. The bed snow properties (M = 0.7, β = 0.4, ξ = 0.1, p_0^{ini} = 12 kPa) in the four cases are identical. Videos of the simulated 4 scenarios in 2D and 3D can be found in the supplementary material. The four groups of released snow properties are determined with reference to the systematic study by Li et al. [17,18], where four snow avalanches in different scenarios and typical flow regimes (i.e. cold dense, warm shear, sliding slab, and warm plug) were captured with 2D and 3D simulations in [17,18], respectively. The avalanches in scenarios 1&2 behave as fluids or cohesionless granular flows. Compared to the avalanche in scenario 1, the avalanche in scenario 2 contains bigger snow granules, mainly contributed from the higher friction and cohesion. Quantitative description of the range of granule sizes would require sophisticated post-processing tools and is not conducted in this study. The motion of the avalanches in scenarios 3&4 is similar to the sliding down of solid objects on the slope, as both of them have relatively high cohesion. Brittle fracture is prevalent in the avalanche in scenario 3 while ductile behavior dominates in scenario 4.

For the snow in the erodible bed, the hardening factor ξ and the initial consolidation pressure p_0^{ini} are kept constant at 0.1 and 12 kPa, respectively. To examine the influence of friction and cohesion of the bed snow, the friction coefficient M and tension/compression ratio β are varied systematically, from 0.3 to 1.5 and from 0 to 1 respectively. The density (250 kg/m^3), Young's modulus (3 MPa) and Poisson's ratio (0.3) are identical for the snow at the release and in the erodible bed.

In addition to the snow properties, the lengths of the release zone and the erodible bed (L_r and L_e in Fig. 2) are changed to study the effect of release size and availability of erodible snow. Note that the front of the release zone and the tail of the erodible bed are fixed when L_r and L_e are varied, respectively. The initial heights of the release zone and the erodible bed are both fixed to 2 m. When investigating the effect of the snow properties, the release length L_r and erodible bed length L_e are 15 m and 40 m, respectively.

3. Results

In interpreting the results, we follow the definitions of *erosion* and *entrainment* in [7], by which the entrained mass is part of the initially eroded mass. Various erosion patterns and temporal evolution of mass change rate in the erodible zone will be discussed first. The distinct effect of snow properties (at release and in the erodible bed) on entrainment and erosion will then be presented. Finally, the opposite effects of erosion on the avalanche mobility reflected by momentum and runout distance will be explored.

3.1. Erosion pattern and mass change rate

With the four sets of release properties, distinct erosion patterns are identified as shown in Fig. 2, where both 2D and 3D simulation results are presented. Compared with the 2D cases, the 3D simulations resolve variations across the width of the flow, and give similar erosion patterns as in 2D. In comparison to the erosion mechanism defined according to the interaction between an avalanche and an erodible bed [7], the erosion pattern termed in this study further accounts for the avalanche features during erosion in addition to the avalanche–bed interaction. Moreover, simulations with no erodible bed were carried out to confirm that the features in the 4 cases in Fig. 2 are indeed due to the interaction between the erodible bed and the incoming avalanches, as the avalanche behavior differs much without the erodible bed. For instance, there are no surges developed in case 1 without the erodible bed (please see the supplementary videos).

When the avalanche behaves as a cohesionless granular flow in scenario 1 (e.g. case 1 in Fig. 2), multiple surges are observed during the erosion. This wavy erosion pattern shares similar characteristics with the scour pattern of debris flows observed in experiments [29]. After the flow enters the erodible bed, its velocity first diminishes as the flow erodes and ploughs into the bed, and then increases as the flow

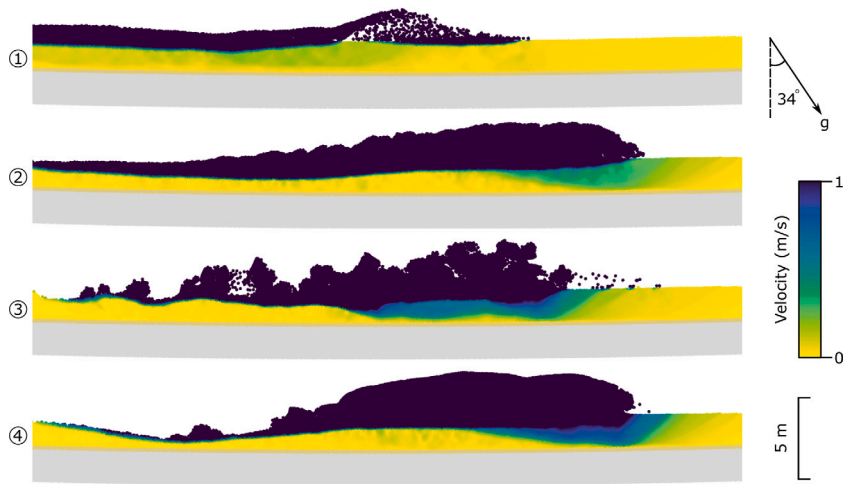

Fig. 3. Frontal erosion and basal abrasion observed in the simulated 4 scenarios in Fig. 2. The average slope angle of the erodible zone is 34°.

moves toward the bed surface and downward the slope. Similar waves were also observed from laboratory experiments on granular flows composed of glass beads [10]. Analogously to the waves developed due to flow instability [34,35], the intermittent surges captured in this study come from the perturbation induced by the erodible bed. The wavy erosion pattern may disappear if the released snow becomes more frictional and cohesive. As shown in case 2 in Fig. 2, the surges tend to vanish in scenario 2. Compared to case 1, the higher snow friction and cohesion in case 2 lead to less separation and lower instability of the snow particles after the avalanche enters the erodible bed and thus result in weaker surges. If the released snow is highly frictional and cohesive, as in scenario 3, it slides down the slope as a slab and breaks into smaller pieces after colliding with the erodible bed (e.g. case 3 in Fig. 2). This collision process and the avalanche movement towards the downstream direction lead to the notable erosion. When the released snow has low brittleness and develops into a plug flow in scenario 4 (e.g. case 4 in Fig. 2), the avalanche is highly cohesive and ductile. The erosion pattern looks similar to that observed in case 2 (as shown in Fig. 3). Compared to case 2, the avalanche in case 4 entrains much more snow near the upstream end of the erodible bed, which might be due to the larger flow depth and concomitant higher shear stress acting on the erodible bed.

In the four simulated scenarios, both frontal ploughing and basal abrasion, as usually identified for snow avalanches [1], are observed (see supplementary videos 3~6). Fig. 3 shows the representative features of the frontal ploughing and basal abrasion in the four scenarios. The illustrated range of velocity in Fig. 3 is determined to clearly demonstrate the interface between stationary and moving particles. The frontal ploughing in case 1 is not as notable as in the other three cases, which might be related to its smaller flow height at the front. The scattered particles at the front in case 1 seldom plough the erodible bed, it is the frontal particles in the continuous main body that primarily contribute to the ploughing behavior. This saltating front with the scattered particles in case 1 was also observed in experiments of dry cohesionless granular flows on an erodible zone [36]. The front ploughing in cases 2~4 show similar characteristics. For bed particles located downstream of (and close to) the flow front, even if there is no direct interaction with the avalanche, they become unstable due to the frontal ploughing and form inclined shear and compaction surfaces. In addition to frontal ploughing, basal abrasion also occurs in the four scenarios. Compared to the smooth interface between the avalanche and the stable bed particles in cases 1,2&4, the interface in case 3 is more irregular, because of the discrete snow fragments in the avalanche and their collisions with the erodible bed.

To evaluate the mass change in the erosion zone throughout the flowing process, the erosion rate q_{er}, entrainment rate q_{en}, and deposition rate q_d, defined as follows, are quantitatively examined in Fig. 4.

$$q_{er} = \frac{m_{er}}{A_{bed} \times \Delta t} \tag{4}$$

$$q_{en} = \frac{m_{en}}{A_{bed} \times \Delta t} \tag{5}$$

$$q_d = -\frac{m_d}{A_{bed} \times \Delta t} \tag{6}$$

where m_{er}, m_{en}, and m_d are the eroded mass, entrained mass, and deposited mass at the erodible bed in the time interval of Δt, respectively. A_{bed} is the initial surface area of the erodible bed. We do not use the instantaneous contact area between the flowing avalanche and the erodible bed as it is difficult to be quantitatively evaluated in our simulations. The time interval Δt is set to 1/12 s. At a certain time instant, a snow particle in the erodible bed is counted as eroded if its displacement from the initial position is larger than 0.5 m. The displacement criterion of 0.5 m is determined with consideration of the grid size (0.1 m) in the MPM simulation. Small variations of this threshold (e.g. to 0.4 m or 0.6 m) lead to different erosion rates, but give the same trends and conclusions. On top of the displacement criterion, an entrained snow particle is recognized as such if its final position is outside of the erodible bed. A snow particle initially in the avalanche is included into the deposited mass m_d if its final position is within the erodible bed and it is currently in the erodible bed with a velocity smaller than 0.1 m/s.

Fig. 4 shows the mass change rates in the erodible bed with the different incoming avalanches simulated. Due to the distinct behaviors of the incoming avalanches, the local characteristics of the mass change rate vary notably. The two spikes in the evolution of the erosion rate q_{er} and entrainment rate q_{en} in Fig. 4a correspond to the two surges observed in scenario 1 (see case 1 in Fig. 2). The spikes with relatively smaller amplitude in Fig. 4b are consistent with the weaker surges in scenario 2 (see case 2 in Fig. 2). This enhanced erosion due to the occurred surges was also observed from experiments by Mangeney et al. [36], where the vertical motion of the surges helps to push the erodible particles upward and make them join the flow. Only local fluctuations are observed in the other two avalanches in Fig. 4c&d, where no significant surges occur (Fig. 2). Despite the local differences, the general trends of q_{er} and q_{en} in the four cases are similar, as they initially increase upon the arrival of the avalanche fronts at the erodible bed and then decrease shortly after the avalanche fronts leave the erodible bed. Based on field measurements, erosion rates above 200 kg m^{-2} s^{-1} were reported for the very rapid removal of fresh snow at

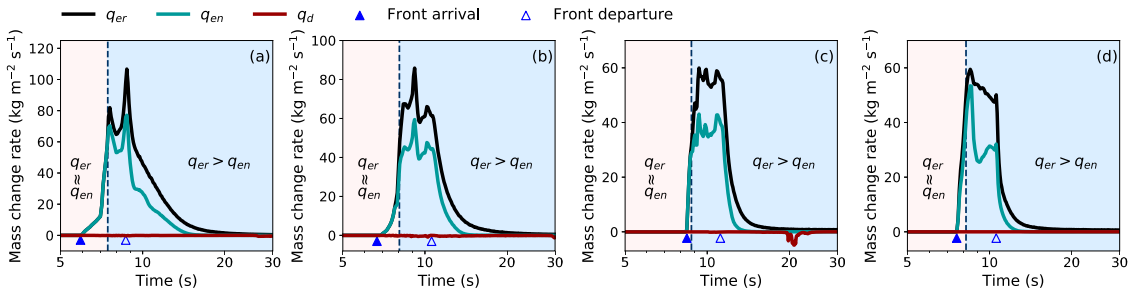

Fig. 4. Mass change rate in the erodible bed for the 4 avalanches in different scenarios simulated in 3D. (a): Scenario 1; (b): Scenario 2; (c): Scenario 3; (d): Scenario 4. The solid and empty triangles mark the instants at which the avalanche front arrives and leaves the erodible bed respectively.

the front of very large avalanches [37], while lower erosion rates of 10~50 kg m^{-2} s^{-1} were documented for more gradual erosion in the head of dry-snow avalanches [7]. The erosion rates obtained in our simulations in Fig. 4 have similar magnitudes with the field data. In the future, more detailed analyses on erosion rate and quantitative comparison with mechanically based entrainment models [38,39] need to be conducted. Furthermore, the deposition rate q_d is very low in all the four cases, mainly due to the steep slope angle of around 35° at the erodible bed. Indeed, there is no obvious deposition observed in the field when a slope is steeper than 35° [13]. It is worth noting that, in all the cases, q_{er} and q_{en} are almost identical at the early stage of the interaction between the avalanche and the erodible bed (i.e. the left side of the dashed line in Fig. 4). This hints that all the eroded snow by the front of the avalanches is entrained into the flow. At a later stage (i.e. to the right of the dashed line in Fig. 4), the lower amount of entrainment, compared with erosion, indicates that only part of the eroded snow gets entrained into the flowing avalanches. This relation between erosion and entrainment throughout the flowing process reveals that the entrainment at and close to the avalanche front is more significant compared to body abrasion, which is in accordance with field experiments [1].

3.2. Entrainment in comparison with erosion

As erosion and entrainment involve different processes, their responses to changing conditions might differ. To evaluate the erosion and entrainment under the effect of varying released snow properties and erodible bed properties, systematic 2D simulations were conducted. The entrained mass and eroded mass throughout the flowing process are shown in Fig. 5, where the criteria of displacement and final position detailed in Section 3.1 are used for calculating the entrainment and erosion. M and β in Fig. 5 respectively characterize the friction and cohesion of the snow in the erodible bed.

The insets in Fig. 5 show the representative effect of the bed snow properties, fixing the properties of the released snow (giving an avalanche in scenario 2). The dashed line in the inset is the linear fitting of the boundary cases with initially stable and unstable beds. When the bed snow friction and/or cohesion are relatively low, the snow moves under gravity and the erodible bed is initially unstable, a condition indicated by the cross symbols in the insets. On the other hand, extremely high friction and/or cohesion prevent erosion and entrainment, as indicated by the black dots in the insets. Notable occurrence of erosion and entrainment requires intermediate values of friction and cohesion of the bed. The cases with significant entrainment in the inset of Fig. 5a form a thin band, within which the color change does not show a clear trend, indicating the obscure effect of bed snow properties on the entrained mass. In contrast, the color variation in the inset of Fig. 5b reveals a clear correlation between the eroded mass and the bed snow properties. When the friction M and/or cohesion β of the bed snow increase, the eroded mass tends to decrease.

The different responses of eroded mass and entrained mass to the change of bed snow properties remain true for other types of incoming avalanches (e.g. in scenarios 1,3,4), as demonstrated by the main figures in Fig. 5. The function $f(M,\beta)$ is the distance from a datum point to the dashed line separating the cases with initially stable and unstable beds in the inset of Fig. 5a or b. This distance reflects the combined effect of snow friction and cohesion.

$$f(M,\beta) = 0.85M + 0.53\beta - 0.82 \tag{7}$$

When the amount of entrainment and erosion is large, the relation between the entrained mass and the bed snow properties is unclear (Fig. 5a). In comparison, the eroded mass has a negative correlation with the bed snow friction and cohesion (Fig. 5b) for the different incoming flows in the 4 scenarios. Apart from the effect of the bed snow properties, Fig. 5 reveals the influence of released snow type (and thus incoming flow type) on the entrainment and erosion. In Fig. 5a, the superposition of the data from different incoming flows hints the negligible effect of the released snow type on the entrained mass. In contrast, the eroded mass in Fig. 5b shows a general trend that scenario 4 > scenario 3 > scenario 2 > scenario 1. This tendency might be

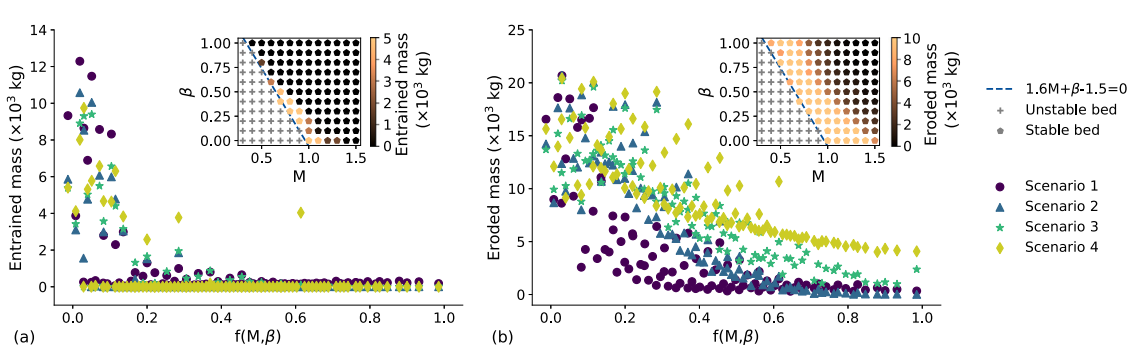

Fig. 5. (a) Entrained mass and (b) eroded mass with various incoming flow types and erodible bed properties (M: snow friction, β: snow cohesion). The insets show the effects of M and β on the (a) entrained and (b) eroded mass when the released avalanche is in scenario 2. (For interpretation of the references to color in this figure legend, the reader is referred to the web version of this article.)

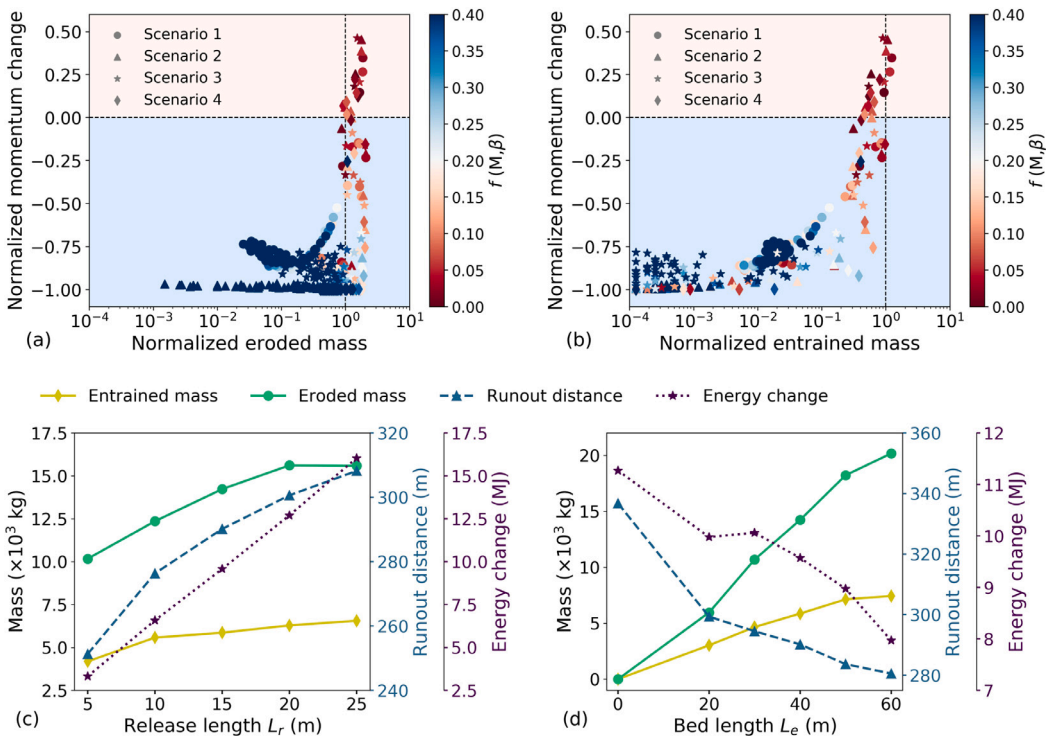

Fig. 6. (a) Evolution of normalized momentum change with normalized eroded mass; (b) Evolution of normalized momentum change with normalized entrained mass; (c) Entrained and eroded mass in positive correlation with runout distance and change of energy (including potential and kinetic energy) when the release length is varied; (d) Entrained and eroded mass in negative correlation with runout distance and energy change when bed length is changed. (For interpretation of the references to color in this figure legend, the reader is referred to the web version of this article.)

related to the cohesion of the released snow (reflected by β listed in Fig. 2). The more cohesive the snow of the incoming avalanche, the more significant the erosion. It is noticed that there is a scattered data point (i.e. $f(M,\beta) = 0.61$) in Fig. 5a in the group of scenario 4, which denotes a rare and special case that the incoming plug flow rolls down the erodible bed and develops into a large snow ball [25].

3.3. Enhanced and inhibited avalanche mobility by erosion

During erosion and entrainment, two processes may contrarily affect the mobility of an avalanche: the avalanche loses momentum during the breaking of the snow cover and the subsequent acceleration of the snow fragments to avalanche speed, but gains momentum due to conversion of the potential energy of the entrained snow into kinetic energy. Although both of the two processes have been widely recognized for snow avalanches, erosion and entrainment have been primarily associated with increased runout distance. In this study, by varying the bed snow properties (i.e. M and β) and the geometry of the release and erodible zones (i.e. L_r and L_e), both the growth and the reduction of the avalanche momentum and runout distance are captured as shown in Fig. 6.

Fig. 6a&b show the momentum change from the inlet to the outlet of the erodible bed, normalized by the avalanche momentum at the inlet of the erodible bed. Positive and negative momentum changes correspond to enhanced and inhibited avalanche motion, respectively. A normalized momentum change of −1 indicates zero momentum at the outlet of the erodible bed, meaning that the avalanche stops inside the erodible bed. This normally happens when the snow friction and (or) snow cohesion are high, and the avalanche mass entering the erodible bed quickly loses its momentum. To conduct a systematic investigation, a wide range of snow friction (M from 0.3 to 1.5) and cohesion (β from 0.0 to 1.0) has been applied in this study. The combination of extreme snow friction and cohesion (e.g. $M = 1.5$ and $\beta = 1.0$) might not be realistic for snow avalanches and can lead to the vanishment of the avalanche momentum. In addition, the stopping behavior depends on the interaction between the flowing avalanche and the erodible bed. As the interaction is based on the background Eulerian grid, with high cohesion and friction of the bed snow, it is similar to having a no-slip boundary condition for the flowing avalanche. The so-called "stickiness" of the interaction in MPM has been recently addressed and solved by Fang et al. [40], which could be used in the future. The eroded and entrained masses in Fig. 6a&b are normalized by the initially released snow mass (i.e. 9920 kg). The colorbar $f(M,\beta)$ reflects the combined effect of snow friction and cohesion (Eq. (7)). According to Fig. 5, a small distance $f(M,\beta)$ tends to give a case with notable erosion and entrainment, while a large distance corresponds to the one with negligible erosion and entrainment. As shown from Fig. 6a&b, erosion and entrainment can either lead to reduction or growth of momentum in cases below or above the horizontal dashed line. While negative momentum change is observed from cases with very little or notable erosion and entrainment, positive momentum change is only obtained from cases with significant erosion and entrainment. When the snow in the erodible bed has small friction M and cohesion β (and thus small $f(M,\beta)$), it is easy to be eroded and entrained. Therefore, the momentum that the avalanche consumes to erode and entrain the bed snow is smaller than the input momentum of the eroded and entrained snow converted from its potential energy, resulting in the increased momentum change and enhanced mobility. The trends in Fig. 6a&b share similar features, where the cases with smaller $f(M,\beta)$ tend to give larger momentum change. The maximum normalized eroded mass in Fig. 6a is 2.09, while the maximum normalized entrained mass in Fig. 6b is 1.24.

In addition to the different changes in momentum, the variation of runout distance due to erosion and entrainment is further investigated by changing the release length L_r and the bed length L_e as shown in Fig. 6c&d. When L_r changes from 5 m to 25 m, the release mass varies from 3298 kg to 16 593 kg. While L_e is changed, L_r is fixed to 15 m, corresponding to a release mass of 9920 kg. Both positive

and negative correlations between erosion/entrainment and runout distance are obtained under the respective effect of L_r and L_e (illustrated in Fig. 2). The runout distance is calculated as the horizontal distance between the fronts of the final avalanche deposit and the initial release zone. With the growth of the release length L_r, the initial potential energy of the released snow increases, offering more energy to erode and entrain the snow in the erodible bed and leading to the growth of eroded mass and entrained mass. Under this condition, the runout distance is positively related to the entrained and eroded mass as shown in Fig. 6c. This positive correlation is attributed to the increase in the potential energy of both the released snow and the entrained snow. On the contrary, entrainment and erosion may have negative effect on the runout distance as well, as illustrated in Fig. 6d. When the length of the erodible bed L_e is longer, there are more snow particles in the bed which can be eroded and entrained, resulting in the growth of the eroded and entrained mass. Meanwhile, the runout distance is reduced, which is tightly associated with the higher bed resistance and the more momentum transfer from the incoming avalanche to the snow in the erodible bed. No matter which correlation occurs between the erosion/entrainment and the runout distance, it is found that the energy change of the avalanches from the outlet of the erodible bed to the avalanche deposit always demonstrate a consistent tendency with the runout distance, as revealed in Fig. 6c&d.

In practice, the runout distance of snow avalanches has been normally positively correlated with erosion and entrainment [1,41]. Indeed, the release volume of real avalanches varies case by case, as well as the properties and the length of the erodible zone (reflecting the supply of the erodible material). The predominantly positive relation between the erosion/entrainment and the runout distance reported from real avalanches indicates the significant role played by the release volume and the snow cover properties compared with the length of the erodible zone. Although the negative correlation between the erosion/entrainment and the runout distance has been seldom recognized for snow avalanches, it was disclosed from similar gravitational mass movements like debris avalanches [42]. The opposite correlations between erosion/entrainment and runout distance in Fig. 6c&d reveal that the growth of erosion and entrainment can enhance or inhibit the avalanche mobility depending on the different conditions. The identification of the opposite mobility changes could rely on physically-based models [8]. It should be noted that, unlike the erodible bed of limited length employed in this study, in reality there usually is erodible snow along the entire avalanche path. The outlet of the erodible zone in practice might refer to the position where entrainment and erosion vanish.

4. Conclusions

By conducting simulations with the material point method, this study has offered new insights into the mechanisms of snow avalanche erosion and entrainment, with special focuses on various erosion patterns, differentiation between erosion and entrainment, as well as their potential influences on avalanche mobility.

Distinct erosion patterns have been captured by using different mechanical properties for the released snow. In addition to front ploughing and basal abrasion, a wavy erosion pattern with multiple surges has been characterized. The analysis of the temporal evolution of mass change rate in the erodible bed serves as a proof for the significant entrainment at and close to the front of snow avalanches.

Notable differences between erosion and entrainment have been identified from the perspective of their relations with properties of released snow and erodible bed snow. The eroded mass tends to be larger when the released snow has more cohesion, while the entrained mass does not show a clear trend. In addition, when notable erosion and entrainment occur, the mass of eroded snow is negatively correlated with the friction and cohesion of the bed snow, while the entrained snow has no obvious tendency.

Moreover, both enhanced and inhibited avalanche mobilities have been captured under different conditions. With varied snow properties in the erodible bed, both the growth and the reduction of the avalanche momentum appear. The increase in the lengths of the release zone and erodible bed results in more erosion and entrainment, but does not necessarily lead to a longer runout distance. Positive and negative correlations between erosion and runout distance are obtained when varying the lengths of the release zone and the erodible bed respectively.

Declaration of competing interest

The authors declare that they have no known competing financial interests or personal relationships that could have appeared to influence the work reported in this paper.

Acknowledgment

J.G. acknowledges financial support from the Swiss National Science Foundation (grant number PCEFP2_181227).

Appendix A. Supplementary data

Supplementary material related to this article can be found online at https://doi.org/10.1016/j.mechrescom.2022.103914.

References

[1] B. Sovilla, P. Burlando, P. Bartelt, Field experiments and numerical modeling of mass entrainment in snow avalanches, J. Geophys. Res.: Earth Surf. (2006) 111.
[2] M. Barbolini, A. Biancardi, F. Cappabianca, L. Natale, M. Pagliardi, Laboratory study of erosion processes in snow avalanches, Cold Reg. Sci. Technol. 43 (2005) 1–9.
[3] M. Teich, P. Bartelt, A. Grêt-Regamey, P. Bebi, Snow avalanches in forested terrain: Influence of forest parameters, topography, and avalanche characteristics on runout distance, Arct. Antarct. Alp. Res. 44 (2012) 509–519.
[4] W. Steinkogler, B. Sovilla, M. Lehning, Influence of snow cover properties on avalanche dynamics, Cold Reg. Sci. Technol. 97 (2014) 121–131.
[5] A. Mangeney, L. Tsimring, D. Volfson, I.S. Aranson, F. Bouchut, Avalanche mobility induced by the presence of an erodible bed and associated entrainment, Geophys. Res. Lett. (2007) 34.
[6] A. Edwards, S. Viroulet, C. Johnson, J. Gray, Erosion-deposition dynamics and long distance propagation of granular avalanches, J. Fluid Mech. (2021) 915.
[7] P. Gauer, D. Issler, Possible erosion mechanisms in snow avalanches, Ann. Glaciol. 38 (2004) 384–392.
[8] Shiva P Pudasaini, Michael Krautblatter, The mechanics of landslide mobility with erosion, Nature Communications 12 (1) (2021) 1–15.
[9] D. Issler, P. Gauer, M. Schaer, S. Keller, Inferences on mixed snow avalanches from field observations, Geosciences 10 (2020) 2.
[10] M. Farin, A. Mangeney, O. Roche, Fundamental changes of granular flow dynamics, deposition, and erosion processes at high slope angles: insights from laboratory experiments, J. Geophys. Res.: Earth Surf. 119 (2014) 504–532.
[11] B. Sovilla, P. Bartelt, Observations and modelling of snow avalanche entrainment, Nat. Hazards Earth Syst. Sci. 2 (2002) 169–179.
[12] M. Eglit, K. Demidov, Mathematical modeling of snow entrainment in avalanche motion, Cold Reg. Sci. Technol. 43 (2005) 10–23.
[13] B. Sovilla, J.N. McElwaine, M. Schaer, J. Vallet, Variation of deposition depth with slope angle in snow avalanches: Measurements from Vallée de la Sionne, J. Geophys. Res.: Earth Surf. (2010) 115.
[14] C. Vera Valero, K.W. Jones, P. Bühler, Release temperature, snow-cover entrainment and the thermal flow regime of snow avalanches, J. Glaciol. 61 (2015) 173–184.
[15] J. Gaume, T. Gast, J. Teran, A. van Herwijnen, C. Jiang, Dynamic anticrack propagation in snow, Nature Commun. 9 (2018) 1–10.
[16] J. Gaume, A. van Herwijnen, T. Gast, J. Teran, C. Jiang, Investigating the release and flow of snow avalanches at the slope-scale using a unified model based on the material point method, Cold Reg. Sci. Technol. 168 (2019) 102847.
[17] X. Li, B. Sovilla, C. Jiang, J. Gaume, The mechanical origin of snow avalanche dynamics and flow regime transitions, Cryosphere 14 (2020) 3381–3398.
[18] X. Li, B. Sovilla, C. Jiang, J. Gaume, Three-dimensional and real-scale modeling of flow regimes in dense snow avalanches, Landslides 18 (2021) 3393–3406.
[19] D. Sulsky, S.J. Zhou, H.L. Schreyer, Application of a particle-in-cell method to solid mechanics, Comput. Phys. Comm. 87 (1995) 236–252.

[20] M. Ghafghazi, D. Shuttle, Accurate determination of the critical state friction angle from triaxial tests, in: Proc. 59th Canadian Geotechnical Conference, Vancouver, 2006, pp. 278–284.
[21] A. Sadrekarimi, S.M. Olson, Critical state friction angle of sands, Géotechnique 61 (2011) 771–783.
[22] J.C. Simo, Algorithms for static and dynamic multiplicative plasticity that preserve the classical return mapping schemes of the infinitesimal theory, Comput. Methods Appl. Mech. Engrg. 99 (1992) 61–112.
[23] J. Simo, G. Meschke, A new class of algorithms for classical plasticity extended to finite strains. Application to geomaterials, Comput. Mech. 11 (1993) 253–278.
[24] J. Ritter, H. Löwe, J. Gaume, Microstructural controls of anticrack nucleation in highly porous brittle solids, Sci. Rep. 10 (2020) 1–10.
[25] A. Stomakhin, C. Schroeder, L. Chai, J. Teran, A. Selle, A material point method for snow simulation, ACM Trans. Graph. 32 (2013) 1–10.
[26] C. Jiang, C. Schroeder, J. Teran, A. Stomakhin, A. Selle, The material point method for simulating continuum materials, in: ACM SIGGRAPH 2016 Courses, 2016, pp. 1–52.
[27] C. Kang, D. Chan, Numerical simulation of 2D granular flow entrainment using DEM, Granul. Matter 20 (2018) 1–17.
[28] O. Pouliquen, Y. Forterre, Friction law for dense granular flows: application to the motion of a mass down a rough inclined plane, J. Fluid Mech. 453 (2002) 133–151.
[29] T. de Haas, T. van Woerkom, Bed scour by debris flows: experimental investigation of effects of debris-flow composition, Earth Surf. Process. Landf. 41 (2016) 1951–1966.
[30] C.P. Borstad, D. McClung, Sensitivity analyses in snow avalanche dynamics modeling and implications when modeling extreme events, Can. Geotech. J. 46 (2009) 1024–1033.
[31] T. Feistl, P. Bebi, M. Teich, Y. Bühler, M. Christen, K. Thuro, P. Bartelt, Observations and modeling of the braking effect of forests on small and medium avalanches, J. Glaciol. 60 (2014) 124–138.
[32] P. Gauer, Considerations on scaling behavior in avalanche flow along cycloidal and parabolic tracks, Cold Reg. Sci. Technol. 151 (2018) 34–46.
[33] P. Gauer, Comparison of avalanche front velocity measurements and implications for avalanche models, Cold Reg. Sci. Technol. 97 (2014) 132–150.
[34] Y. Forterre, O. Pouliquen, Long-surface-wave instability in dense granular flows, J. Fluid Mech. 486 (2003) 21–50.
[35] S. Viroulet, J. Baker, F. Rocha, C. Johnson, B. Kokelaar, J. Gray, The kinematics of bidisperse granular roll waves, J. Fluid Mech. 848 (2018) 836–875.
[36] A. Mangeney, O. Roche, O. Hungr, N. Mangold, G. Faccanoni, A. Lucas, Erosion and mobility in granular collapse over sloping beds, J. Geophys. Res.: Earth Surf. (2010) 115.
[37] D. Issler, Experimental information on the dynamics of dry-snow avalanches, in: Dynamic Response of Granular and Porous Materials under Large and Catastrophic Deformations, Springer, 2003, pp. 109–160.
[38] D. Issler, Dynamically consistent entrainment laws for depth-averaged avalanche models, J. Fluid Mech. 759 (2014) 701–738.
[39] D. Issler, Comments on on a continuum model for avalanche flow and its simplified variants by SS grigorian and AV ostroumov, Geosciences 10 (2020) 96.
[40] Y. Fang, Z. Qu, M. Li, X. Zhang, Y. Zhu, M. Aanjaneya, C. Jiang, IQ-MPM: an interface quadrature material point method for non-sticky strongly two-way coupled nonlinear solids and fluids, ACM Trans. Graph. 39 (2020) 51.
[41] J. Schweizer, C. Mitterer, L. Stoffel, On forecasting large and infrequent snow avalanches, Cold Reg. Sci. Technol. 59 (2009) 234–241.
[42] S. Cuomo, M. Pastor, L. Cascini, G.C. Castorino, Interplay of rheology and entrainment in debris avalanches: a numerical study, Can. Geotech. J. 51 (2014) 1318–1330.